RESEARCH ARTICLE

Interplay of the leading-edge vortex and the tip vortex of a low-aspect-ratio thin wing

Lei Dong[1] · Kwing-So Choi[1] · Xuerui Mao[1]

Abstract

Three-dimensional vortical structures and their interaction over a low-aspect-ratio thin wing have been studied via particle image velocimetry at the chord Reynolds number of 10^5. The maximum lift of this thin wing is found at an angle of attack of 42°. The flow separates at the leading-edge and reattaches to the wing surface, forming a strong leading-edge vortex which plays an important role on the total lift. The results show that the induced velocity of the tip vortex increases with the angle of attack, which helps reattach the separated flow and maintains the leading-edge vortex. Turbulent mixing indicated by the high Reynolds stress can be observed near the leading-edge due to an intense interaction between the leading-edge vortex and the tip vortex; however, the reattachment point of the leading-edge vortex moves upstream closer to the wing tip.

Graphic abstract
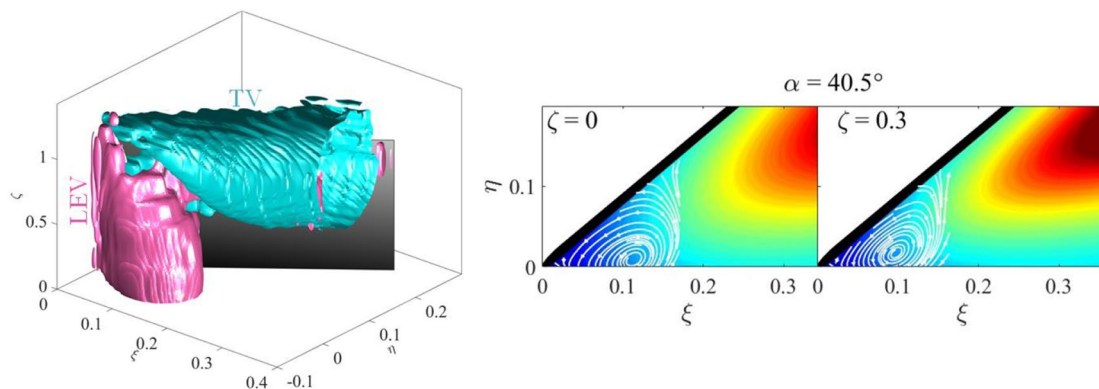
1 Introduction

Low aspect-ratio (AR) wings have been designed for micro-air-vehicles (MAVs) to meet their special requirements. Comparing to conventional wings, they have a high stall angle that improves the manoeuvrability of the aircraft. Flow structures around low AR wings are quite different from high AR wings or two-dimensional aerofoils because of the short span length, resulting in an intense interplay between the leading-edge vortex (LEV), the trailing-edge vortex (TEV) and the tip vortex (TV). The imbalance of pressure distribution makes the flow at the wing tip-edge move from the pressure side toward the suction side, after the incoming flow is separated at the tip-edge.

A similar geometrical wing can be found in some natural creatures, such as flies, insects and bats. To investigate the aerodynamic mechanism behind this, the flow visualization and particle image velocimetry (PIV) techniques were used to observe the flow field around those creatures and four types of vortices including the LEV, the TEV, the TV and the root vortex were identified, contributing collectively to the lift production (Willert and Gharib 1997; Warrick et al. 2005b; Bomphrey et al. 2009a; Carr et al. 2013b; Von Ellenrieder et al. 2003a). There were some common

✉ Kwing-So Choi
  kwing-so.choi@nottingham.ac.uk

1 Faculty of Engineering, University of Nottingham, Nottingham, UK

characteristics between the MAVs and the creatures. Normally, wing flapping comprises of three kinds of kinematics motions—rotation, pitching, and plunging (Wang 2005a). In the process of these motions, large-scale vortices could be formed, contributing to the lift production (McCroskey 1982b; Ohmi et al. 1991b; Yilmaz and Rockwell 2012). However, the formation and stability of the LEV are sensitive to parameters like the Reynolds number (Re), pitching angle, etc (Shyy and Liu 2007a). Baik et al. (2012) considered the effect of the Re and the reduced frequency on the formation of the LEV during the downstroke of a wing using PIV measurements. The results showed that the influence of the Re may be ignored since the reduced frequency could dictate the LEV formation at a higher frequency. Granlund and Bernal (2011b) used a thin plate with AR = 3.4 to study the LEV and TEV formation with different stroke-to-chord ratios. They found that vortical structures in the wake region were much simpler at a large stroke-to-chord ratio but thrust coefficients were almost identical to a two-dimensional plate. Bohl and Koochesfahani (2009b) examined vortical structures of an airfoil via molecular tagging velocimetry at a low pitching amplitude (2°) with a high pitching rate. They concluded that the orientation of the vortex array varied with different pitching rates and the positive circulation would transfer from below to above. PIV technique was used to study the wake behind an airfoil with different Strouhal numbers (St) (Von Ellenrieder and Pothos 2008b). They found that the wake started to be deflected and asymmetric velocity profile was obtained when the St was greater than 0.434.

A wide range of experiments and computations of unsteady aerodynamics of two-dimensional (2D) models have improved our understanding of the lift enhancement on a flapping wing. However, as noted above, a short span length makes the TV interact intensely with the LEV and TEV. This creates complex three-dimensional (3D) flow structures, which is fundamentally different from a 2D counterpart. The TVs of low AR aerofoils are similar to the LEVs of delta wings (two counter-rotating vortices are generated from separated flow at the swept leading-edge) that usually have a deep stall angle (Visbal 1994b; LeMay et al. 1990a). To make it clear about the role of the TV on the lift contribution, some investigations of 3D flow structures over low AR wings have been conducted (Carr et al. 2013b; Yilmaz and Rockwell 2012; Taira and Colonius 2009a; Hartloper et al. 2013a; DeVoria and Mohseni 2017b). Taira and Colonius (2009a) studied the unsteady vortices dynamics of wings with different ARs (1, 2 and 4) and geometries (rectangular, elliptic semicircular and delta) at the Re of 300 and 500. The wake of the wing was different depending on the AR and angle of attack (AoA): (i) a steady state, (ii) a periodic unsteady state and (iii) an aperiodic unsteady state. The platform geometries could modify the TVs to stabilise the flow and interact with the shedding vortices. Development

of vortical structures around the rectangular and elliptical planforms during the pitching period at AR = 2 was investigated by Yilmaz and Rockwell (2012). Their results showed that a strongly 3D flow and the spanwise vorticity dominated near the platform at high AoAs. Carr et al. (2013b) focused on the flow behaviour of coherent LEV, TV and TEV of wings with two ARs (2 and 4) under rotating motion. They observed that lower AR wings contained stronger spanwise vorticity and velocity with a "four-lobed" distribution. DeVoria and Mohseni (2017b) experimentally studied the interplay between the TV and the TEV over a wing at a high incidence at various ARs from 0.75 to 2.5. They confirmed that a downwash coming from the TV would merge with the TEV to help maintain the Kutta condition, which is the reason why the lift is still sustained at a high AoA.

Although there are some investigations on vortex dynamics on a low AR platform, the interplay of the LEV and the TV still remains elusive. In the present work, we pay attention to the interactions between the LEV and TV and their contributions on the lift generation at a very low AR of 0.26 via PIV and force measurements. To observe the effect of the TV on the leading-edge separation and to study the development of the TV along the streamwise direction, the flow field in two planes (x–y and y–z) were captured, where the λ_2 criterion (Jeong and Hussain 1995b) was used to identify the complex vortical structures. In the following section, the experimental setup is introduced first with a result of aerodynamic force measurement. Then, the interaction between the LEV and the TV at different AoAs are presented. This paper concludes with a discussion of the effect of the induced velocity of the TV in suppressing and reattaching the LEV.

2 Experimental set-up

All experiments were conducted in an open-return wind tunnel with an acrylic clear test section. The cross section of this wind tunnel was 0.9 m × 0.9 m with a test length of 1.5 m. A thin wing of AR = 0.26 was constructed from an aluminium composite sheet with a thickness of 3 mm and an elliptical edge was attached to the leading edge of the wing to avoid the flow separation as shown in Fig. 1. The chord length was c = 260 mm and the half-span length was s = 35 mm, giving a thickness-to-chord ratio of 1%. The freestream velocity, U_∞, was set to 6.35 m/s, corresponding to Re = 10^5 based on the chord length. To promote the transition to turbulence near the leading-edge of the wing, a turbulence grid was installed upstream of the test section, therefore the freestream turbulence intensity reached 4%. This increased the effective Re, which was approximate 1.5×10^6 in this experiment (Wang et al. 2014b). We have only focused on the top half of this symmetric wing. The

Fig. 1 Diagram of the thin wing dimension not to scale, plan view (top) and side view (bottom). All dimensions are in millimetres. The coordinate system and origin are shown here
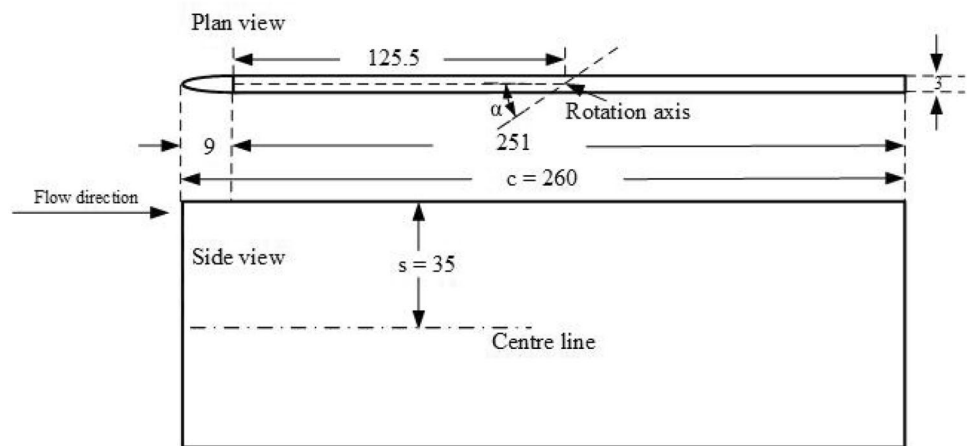
coordinate system is defined along the streamwise direction (x in streamwise direction, y in cross-flow direction and z in spanwise direction). U, V and W denote the mean velocity components in x, y, and z directions, respectively.

The test model was installed on a three-component balance that connected to a step motor, giving a step angle of $0.09° \pm 5\%$, giving precise control of the AoAs. In this research, six AoAs (α) were tested, including 0° (0 step), 10.8° (120 steps), 20.7° (230 steps), 30.6° (340 steps), 40.5° (450 steps) and 50.4° (560 steps). The rotation axis was located at $0.52c$ of the test model, see Fig. 1. Even at the largest AoA, the blockage was only 1.8%. Therefore its impact was not considered in this work. The lift and drag forces on the wing were measured using a three-component strain gauge balance (Kyowa LSM-B-SA1) with a natural frequency of 800 Hz. The absolute accuracy of this strain gauge was less than ± 0.02 N. The outputs of the strain gauge were amplified using Kyowa DPM-911B Strain-Gauge Amplifier and recorded at 2 kHz using an analogue-to-digital converter and finally stored on a computer. The acquisition time was over $10s$ at every force measurement. The measured forces were normal (F_n) and parallel (F_p) to the wing, since the force balance was rotated with the wing as the AoA was changed. Therefore the lift force F_L and the drag force F_D could be calculated as $F_L = F_n cos(\alpha) - F_p sin(\alpha)$ and $F_D = F_n sin(\alpha) + F_p cos(\alpha)$, respectively.

The velocity field around the thin wing was measured using a two-dimensional PIV system, comprising of a Litron LDY302-PIV Nd:YLF laser with 15 mJ per pulse, a CMOS high-speed camera with a spatial resolution of 1280 pixels × 800 pixels and a dedicated PC. Di-ethyl-hexyl-sebacate (DEHS) particles generated by a TSI 9307-7 seeder were used to trace the velocity. The diameter of DEHS was nominally less than 0.3 µm and two generators were used upstream of the wind tunnel contraction section to generate a uniform particle field. On a low AR wing, the TEV could be impeded by the TV, resulting in vanishingly

small velocity and vorticity field downstream (DeVoria and Mohseni 2017b). Thus, we mainly concentrated on the front (upstream) section of the wing with a 100 mm focal length lens. To obtain the velocity field in the x-y plane, the laser sheet was parallel with the freestream with a sheet thickness of 0.5 mm, where the camera was fixed on the top of the wind tunnel, see Fig. 2. The field of view was $0.5c$ (x-axis)×$0.25c$ (y-axis). For the y–z plane, an 8 cm × 8 cm mirror was placed downstream at 45° to the freestream so that the camera was set outside of the wind tunnel. Here the laser sheet was perpendicular to the freestream with an expanded sheet thickness of 2.5 mm. The field of view in this case was set to $0.4c$ (y-axis)×$1.5s$ (z-axis). The measured distance from leading-edge along the chord was kept constant at all AoAs, which was $0.4c$. The twin-cavity laser was operated with a time delay of 50 µs between the two consecutive pulses at the repetition rate of 200 Hz and a total of 400 image pairs were recorded continuously for both cases. The
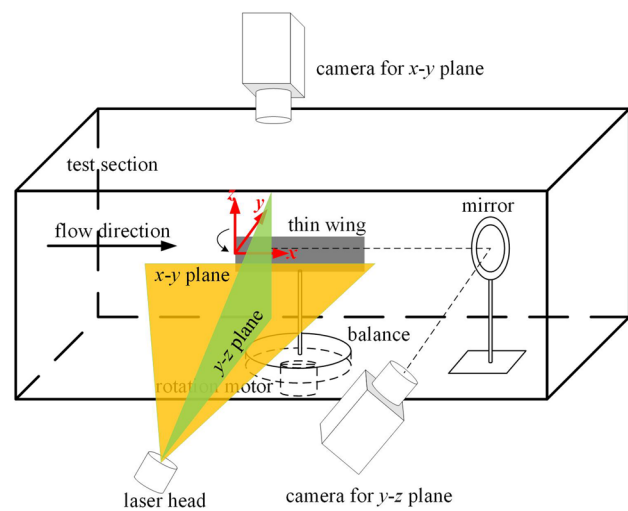

Fig. 2 Sketch of the force measurements and PIV experimental set-up

distance between neighbouring planes in either spanwise or streamwise was 5 mm. Particle images were processed using Dantec DynamicStudio 2015a software. An adaptive PIV algorithm was applied to compute the velocity vector and the minimum and maximum interrogation areas were set as 16 and 64 pixels with a 50% overlap. An universal outlier detection analysis was applied to remove the spurious vectors Westerweel and Scarano (2005b). Any invalidated vectors were replaced by the median vector calculated using 3×3 neighborhood vectors, which finally generated about 4000 vectors in total in each frame.

Uncertainty in velocity measurements using PIV is estimated by $U_e = \sqrt{\frac{D_e^2}{T^2} + (-\frac{D}{T^2})^2 T_e^2}$ (Kine and McClintock 1953), assuming that its primary sources of error are the shift distance D of seeding particles and the interval time T between image pairs. Here, D_e is the uncertainty in particle shift distance, which is about 0.15 pixel. The uncertainty in the interval time T_e between image pairs is negligible. This gives $U_e = 0.33$ m/s or $U_e/U_\infty = 5.2\%$, which is similar to the PIV measurements error estimated by Westerweel (1997a).

3 Results and discussions

3.1 Overview of the flow around a low AR wing

The lift coefficient $C_L = F_L / \frac{1}{2}\rho U_\infty^2 A$ and drag coefficient $C_D = F_D / \frac{1}{2}\rho U_\infty^2 A$ of a low-aspect-ratio thin wing at different AoAs are shown in Fig. 3, where ρ is the air density, A is the surface area of wing. Uncertainties in force measurements are on the order of 5% and 3% for C_L and C_D, respectively, which are shown by error bars in Fig. 3. It is known that the lift coefficient C_L of a 2D aerofoil has a constant lift slope for small AoA (Pelletier and Mueller 2000a). However, the highly nonlinear lift curve can be seen on the low AR wing. Meanwhile, comparing to the 2D case, both the stall angle and the C_L of the low AR wing are greater although it requires a high AoA to get the same C_L to the 2D wing. Similar results were obtained by Torres and Mueller (2004b), showing almost the same trend only with a small difference in the stall angle due to different ARs. The delayed stall angle seems to be due to the existence of the TV which can affect the flow structure on a low AR wing (Fig. 4). The C_D on the low AR wing stays low until $\alpha = 8°$ before increasing fast until the stall angle.

Three velocity components (U, V and W) from two separate PIV measurements are combined together to show 3D flow fields around a low AR thin wing. Vortical structures from $\alpha = 0°$ to $\alpha = 50.4°$ are shown in Fig. 4a–f. These vortical structures are identified by the iso-surface of λ_2-criterion (Jeong and Hussain 1995b) representing 4% of its maximum
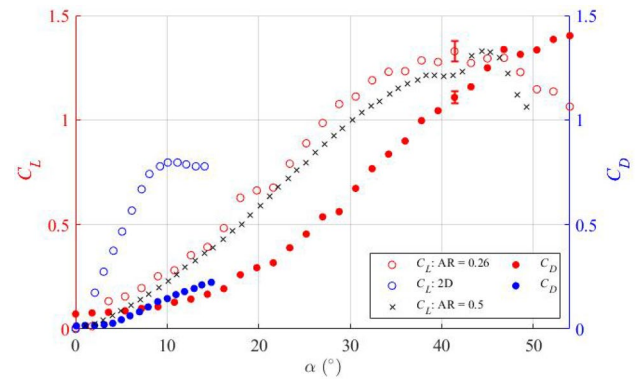

Fig. 3 Force measurements (lift coefficient C_L, left Y-axis and drag coefficient C_D, right Y-axis) of the wing at different AoAs. The hollow circles indicate the C_L of the low AR wing (Re = 10^5, red) and 2D thin aerofoil from Pelletier and Mueller (2000a) (Re = 10^5, blue), while the solid circles represent their C_D; $\times$ C_L on AR = 0.5 wing from Torres and Mueller (2004b) at Re = 10^5. The error bar indicates a standard deviation of the present experimental uncertainty

value. It has been confirmed that this choice of the λ_2 does not affect the identification of vortices in this work. The freestream velocity is along the ξ-axis from left to right in this figure, where the pink and the cyan-blue colours represent the LEV and the TV, respectively. Here, $\xi = x/c$, which represents the distance along the streamwise direction to the leading edge. Similarly, $\eta = y/c$ and $\zeta = z/s$, so that $\eta = 0$ is at the leading edge while $\zeta = 0$ indicates the mid-span of the wing. Note that, the TV is identified by V- and W-component velocities while the LEV is by U- and V-component velocities in each PIV measurement. With an increase in the AoA, the separated flow at the wing tip moves from the pressure side to the suction side, resulting in a TV. Meanwhile, a LEV can be observed near the leading-edge, accompanying a recirculation area. Low pressure on the wing surface can be created by the TV and the LEV to enhance the lift on a wing (Madnia 2010).

For a 2D or a large AR aerofoil, the stall angle is generally less than 20° (Storms and Jang 1994b; Rossow 1978b; Mueller and Batill 1982a). With an increase in the AoA, the flow will start to separate and this separation point will move towards the leading-edge, and then the lift is lost. Interestingly, a stronger LEV can be observed on a low AR wing. The existence of this TV is thought to induce velocity to suppress the leading-edge separation, maintaining the LEV (Taira and Colonius 2009a; Winter 1936b; Jian and Ke-Qin 2004a). At a small angle of attack the LEV is small and nearly uniform in spanwise direction, see Fig. 4b. With an increase in the AoA, the volume of both the LEV and the TV increases (Fig. 4c, d). Near the stall angle the TV starts to expand as shown in Fig. 4e and finally detaches from the wing surface at $\alpha = 50.4°$ (Fig. 4f). In the following, the characteristics of the LEV along the span will be studied

Fig. 4 Vortical structures at different AoAs ($\alpha = 0°$ to $50.4°$). The flow is from left to right along the ξ-axis. Pink structure indicates the LEV while cyan-blue structure indicates the TV
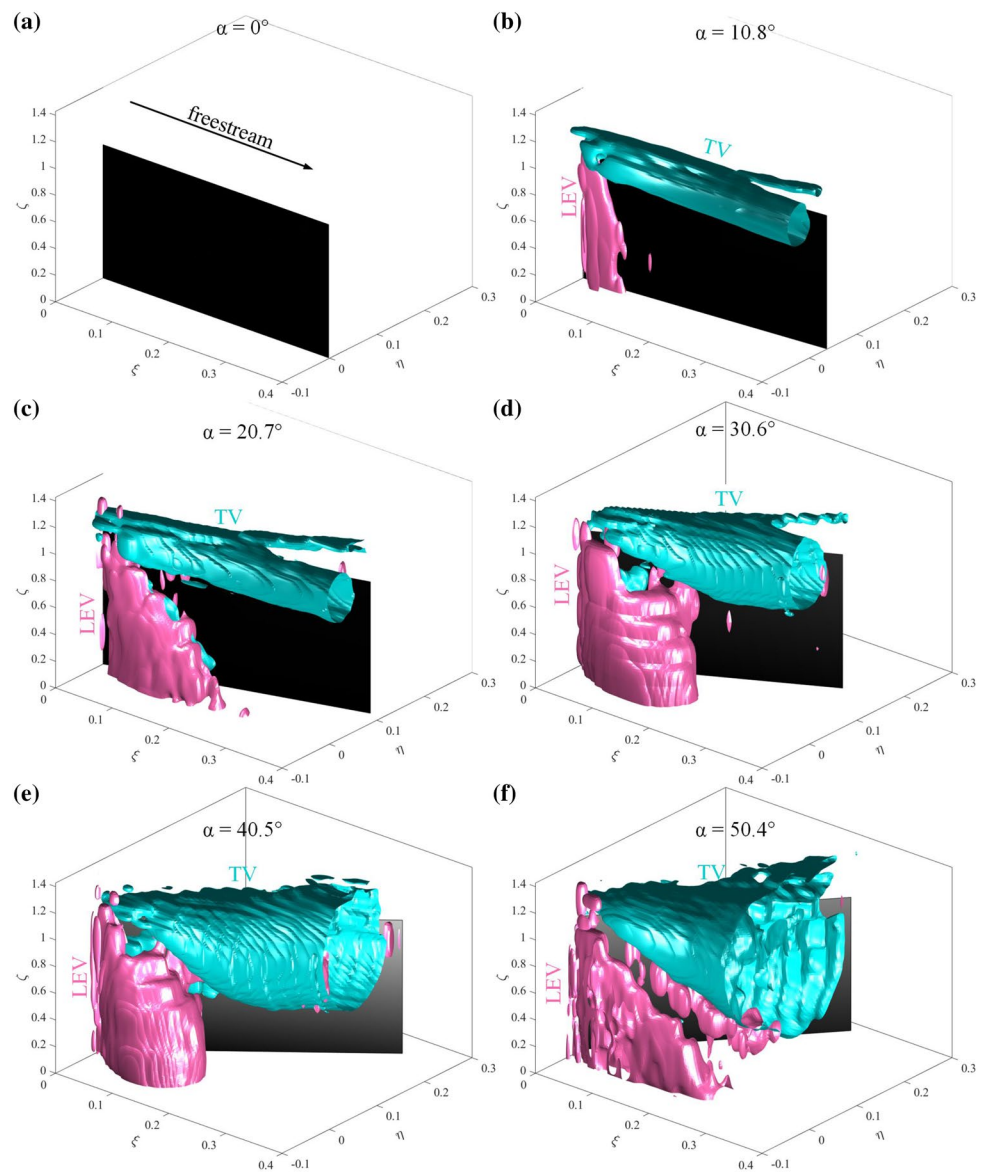
by investigating how the TV affects the separated flow and delays the stall.

3.2 Details of the LEV on a low AR wing

The non-dimensional spanwise vorticity ($\omega_z c/U_\infty$) superimposed on velocity vectors in the x–y plane at different AoAs along the span is shown in Fig. 5. Yellow solid lines and points are the LEVs and their centroids, respectively, which are identified by the λ_2 criterion. Although this criterion may not distinguish the multiple adjacent vortices (Jiang and Machiraju 2005b), it is useful in our study to understand the interaction between the TV and the LEV. Note that the contour of λ_2 here indicates the LEV as well as the shear layer. The thin wing is shown by the thick black line. The chord position of flow structures can be identified by white

markers, which are shown in every 10% chord length along the wing. For small values of AoAs at the mid-span, the LEV can hardly be identified, since the flow is dominated by a shear layer represented by positive vorticity as shown in Fig. 5a. With an increase in the AoA from $\alpha = 20.7°$ to $\alpha = 40.5°$ at the mid-span ($\zeta = 0$), the boundary layer separates at the leading-edge and then reattaches to the wing surface, at $\xi = 0.24$ at $\alpha = 30.6°$ (see Fig. 5i) and at $\xi = 0.2$ at $\alpha = 40.5°$ (see Fig. 5m). This creates a recirculation zone, whose size increases with α. Here, the LEV is clearly identified at $\alpha = 30.6°$ and $\alpha = 40.5°$ as shown in Fig. 5i, m. Downstream of the LEV, the vorticity field is dominated by the wall shear due to the induced velocity by the TV. Moving away from the mid-span, the flow field does not make significant change at $\alpha = 10.8°$. With an increase in the AoA, the separation region becomes smaller and finally vanishes
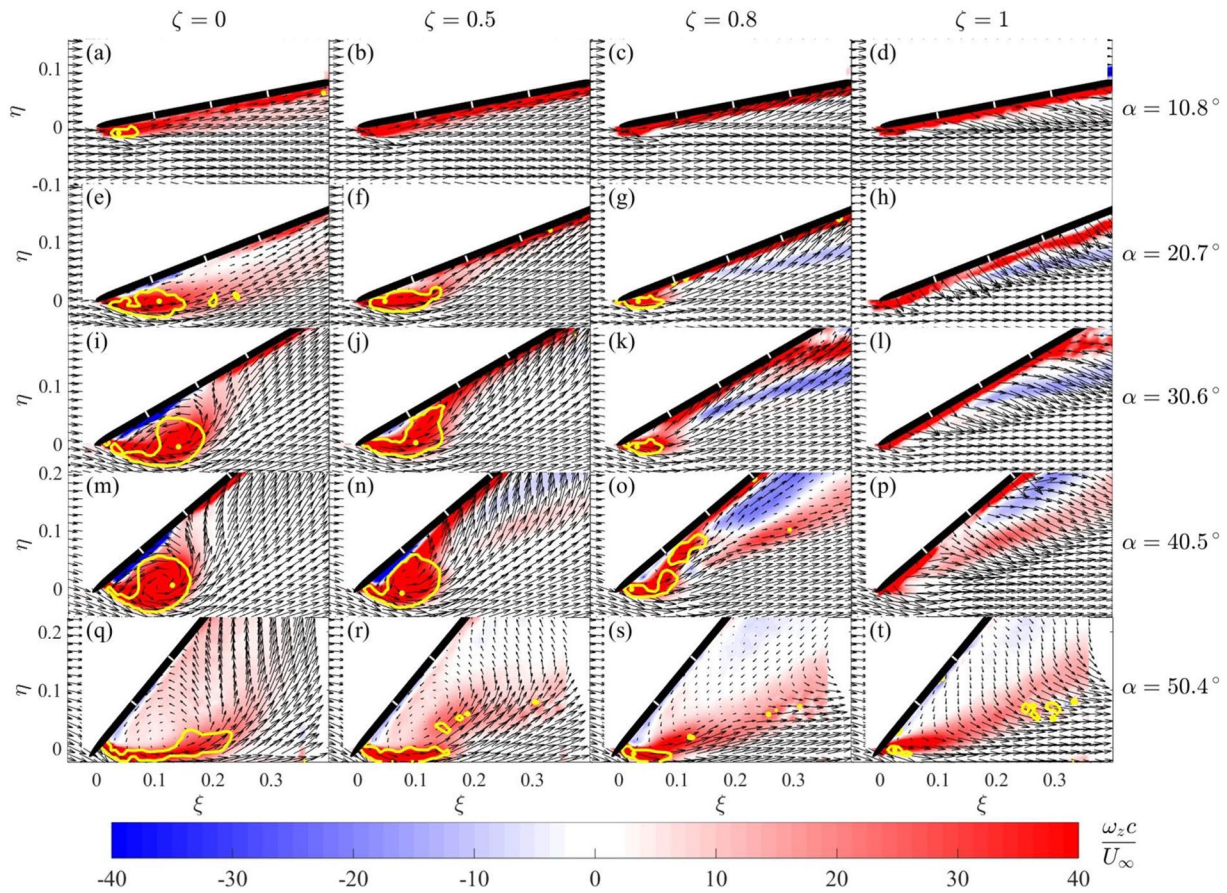
Fig. 5 Vorticity field superimposed on the velocity vectors along the span from $\zeta = 0$ to $\zeta = 1$ at five AoAs ($\alpha = 10.8°$ to $50.4°$). The yellow lines and points in figure indicate the LEVs and the centroids of the LEVs identified by the λ_2−criteria, respectively. White markers are shown in every 10% chord length along the wing

at the wing tip ($\zeta = 1$). At the same time, the LEV centroid moves towards the leading-edge, see Fig. 5g, k, o. Although, the induced velocity by the TV helps reattach the separated flow (Taira and Colonius 2009a; Winter 1936b; Jian and Ke-Qin 2004a), how such an induced velocity controls the separated flow along the span is not fully understood. This will be discussed later.

The time-averaged velocity field as shown in Fig. 5 demonstrates that the separated flow can be suppressed and reattached to the wing surface, forming a compact LEV. To investigate the interplay between the LEV and TV, the turbulence intensity of u' ($u' = \sqrt{\overline{u^2}}/U_\infty$) and v' ($v' = \sqrt{\overline{v^2}}/U_\infty$) and the Reynolds stress ($-\overline{uv}/U_\infty^2$) superimposed by the streamlines are shown in Figs. 6, 7 and 8, respectively. There is a large turbulence intensity region near the leading edge, indicating a strong shear layer. Interestingly, the largest streamwise turbulence intensity can be observed at $\alpha = 30.6°$. The flow behaviour over a low AR wing can be determined by the balance between the flow separation at the leading-edge (negative effect) and the induced velocity by the TV (positive effect), both of them are a function

of the AoA. At small AoAs ($\alpha = 10.8°$ and $\alpha = 20.7°$), the TV is weak, so it cannot help reattach the separated flow completely. Some velocity fluctuations can still be observed even at $\xi = 0.4$. With an increase in the AoA, the strength of the TV is increased, suppressing the leading-edge separation by its induced velocity. This is clearly seen in Fig. 7, where velocity within the leading-edge shear layer is turned towards the wing surface with a strong region of v' on the perimeter of LEV.

Near the stall angle, the intense leading-edge separation cannot be managed by the induced velocity of the TV anymore, so the flow starts to separate and a large wake region can be seen in Fig. 6q. Moving from mid-span to the tip-edge ($\zeta = 1$), there is a strong interaction between the separated flow and the TV, generating intense velocity fluctuations near the leading-edge as shown in Fig. 6k, o as well as in Fig. 7k, 7o. While the u' is generated by the shear layer, the increase in v' is predominantly due to the induced velocity of TV. The strongest v' is observed close to the reattachment point of the separated flow.
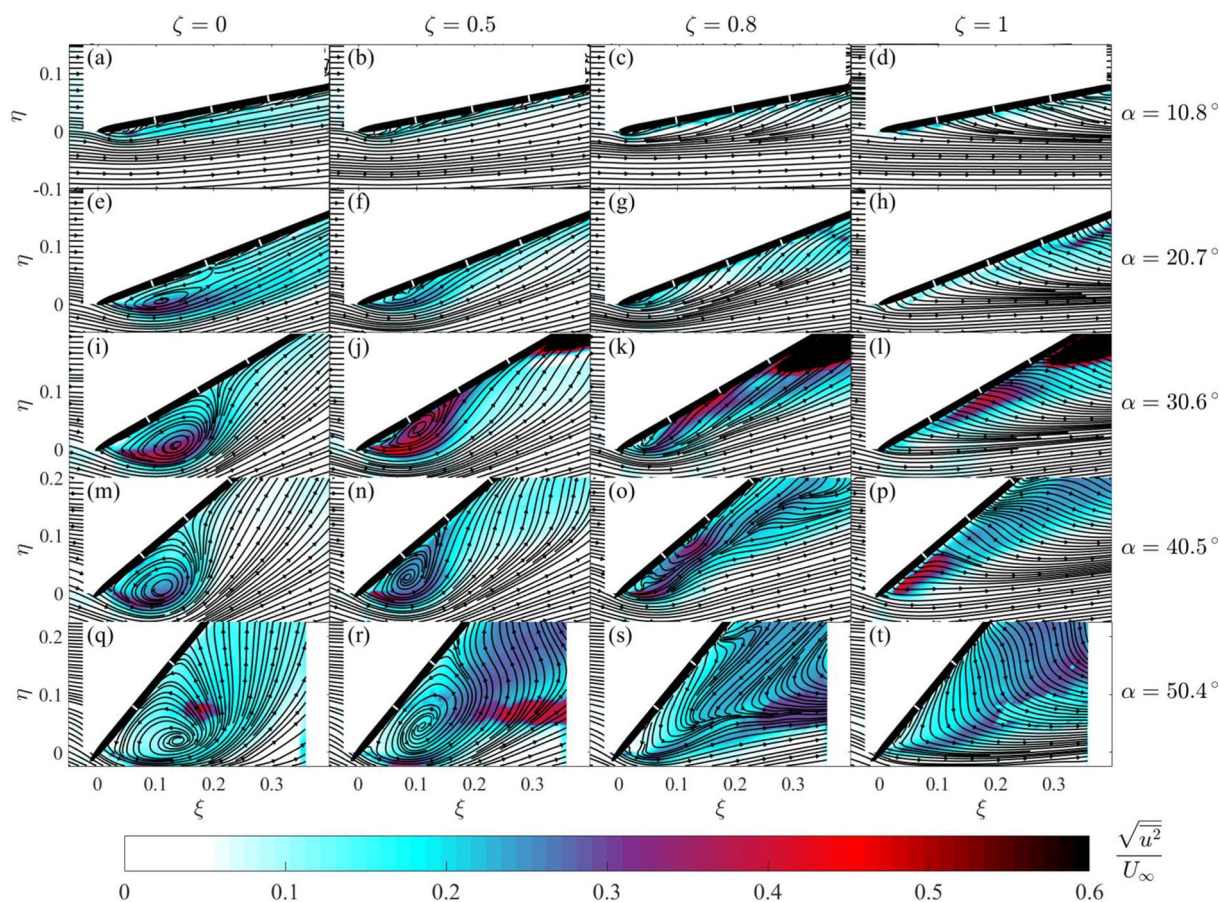
Fig. 6 Non-dimensional turbulent intensity $u' = \sqrt{\overline{u^2}}/U_\infty$ superimposed on the streamlines along the span from $\zeta = 0$ to $\zeta = 1$ at five AoAs ($\alpha = 10.8°$ to $50.4°$). White markers are shown in every 10% chord length along the wing

The turbulent mixing in the shear layer developing from the leading-edge and near the flow attachment region can be indicated by the Reynolds stress $(-\sqrt{\overline{uv}}/U_\infty^2)$ in Fig. 8. At the mid-span, the Reynolds stress increases and reaches its peak along the chord, and then decreases downstream at all AoAs, which is similar in behaviour to backward facing step flows (Chandrsuda and Bradshaw 1981a). This is due to the development of a shear layer from the leading-edge, which could involve shedding vortices. Moving from the mid-span to the tip-edge, the flow reattachment regions have large Reynolds stress, see Fig. 8j, n, k, o, which was not observed in backward facing step flows (Chandrsuda and Bradshaw 1981a). These should be due to the interaction between the LEV and TV, since these areas correspond to the edge of TV cores. At $\alpha = 20.7°$, the TV is small and its induced velocity is weak, see Figs. 10 and 13.

To clarify the contribution of the LEV on the total lift, the non-dimensional circulation $\Gamma_{LEV}{}^* = \Gamma_{LEV}/U_\infty c$ along the span of the positive vorticity inside the LEV is shown in Fig. 9. Only the results at $\alpha = 20.7°$, $\alpha = 30.6°$ and $\alpha = 40.5°$ are shown, where the LEV can be clearly observed. With

an increase of AoA, $\Gamma_{LEV}{}^*$ increases and contributes to the lift on the wing, although it collapses to zero at $\zeta = 1$ at all AoAs. A similar result has been shown by DeVoria and Mohseni (2017b) and Yilmaz and Rockwell (2012). The contribution of the LEV to the total lift is estimated by applying the Kutta-Joukowski's lift theorem on Γ_{LEV}, assuming that the whole leading-edge vortex is symmetric around the mid-span. Results show that the LEV plays an important role on total lift, contributing $27 \pm 7\%$ for $\alpha = 20.7°$ to $40.5°$.

3.3 Details of the TV on a low AR wing

Figure 10 shows the non-dimensional streamwise vorticity $(\omega_x/U_\infty c)$ superimposed on the velocity vectors along the chord in the y–z plane at five AoAs. The solid yellow lines and points indicate the TVs and their centroids of the TVs, respectively, identified by λ_2 criterion. The black rectangles indicate the wing profile viewed from downstream, where the upstream section is made translucent to show the flow field. The velocity vector near the tip-edge moves from the pressure side (right-hand side of the figure) to the suction
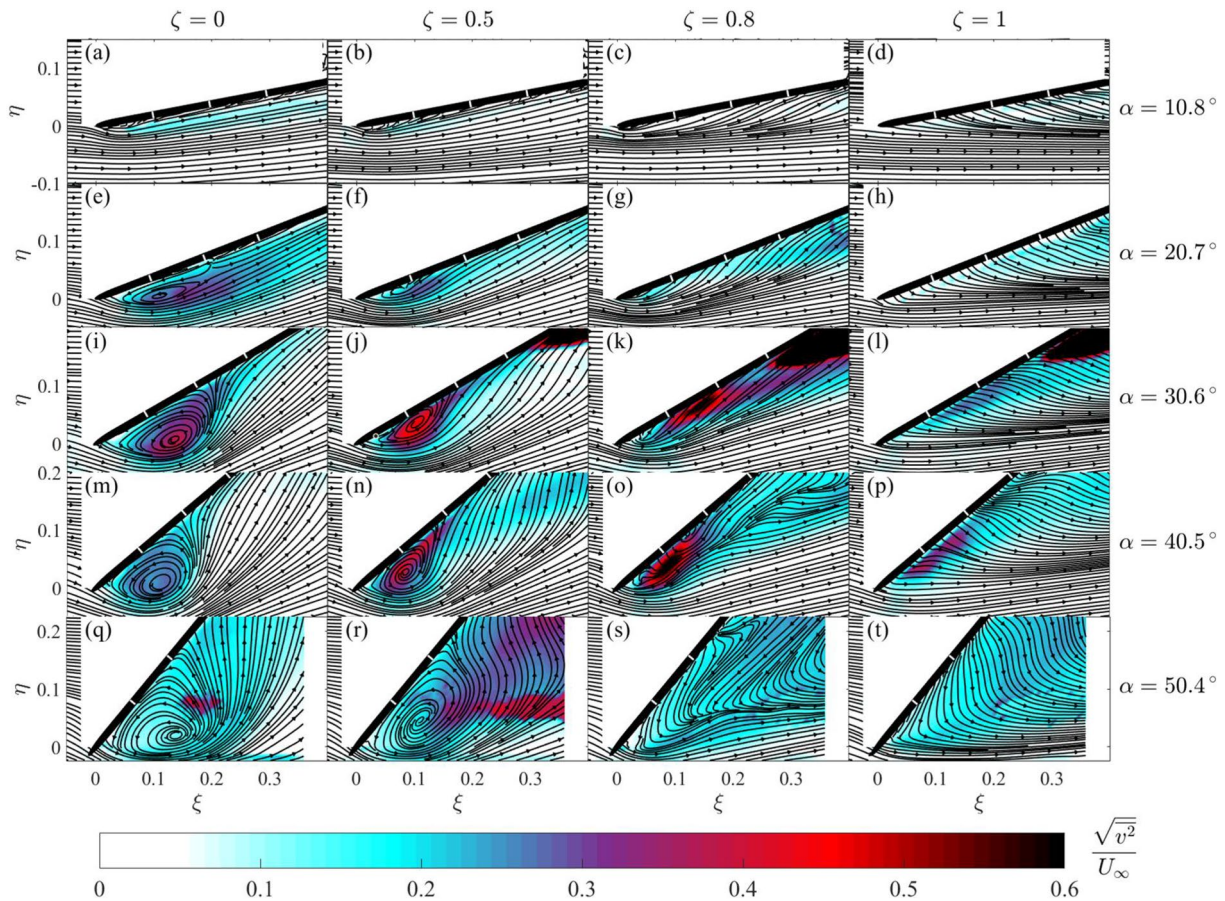
Fig. 7 Non-dimensional turbulent intensity $v' = \sqrt{\overline{v^2}}/U_\infty$ superimposed on the streamlines along the span from $\zeta = 0$ to $\zeta = 1$ at five AoAs ($\alpha = 10.8°$ to $50.4°$). White markers are shown in every 10% chord length along the wing

side (left-hand side of the figure) due to the imbalance of the pressure on the wing surfaces. At a short downstream distance from the leading-edge, the TV is about to form, where the velocity magnitude is still very small as shown in Fig. 10a, e, i, m, q. Meanwhile, another flow motion from the mid-span towards the tip-edge can be found between $\zeta = 0$ and $\zeta = 0.7$, which originates from the LEV. The maximum velocity of this flow can reach to the freestream value near the stall angle as the LEV develops. In Fig. 10j at $\alpha = 30.6°$ and Fig. 10n at $\alpha = 40.5°$, the swirling velocity induced from the TV helps the separated flow reattach to the wing surface. With an increase in the distance to the leading-edge, the velocity associated with the LEV reduces under the effect of the TV as shown in Fig. 10k, o. Moving from the leading-edge towards the trailing-edge of the thin wing, TV's swirling area indicated by a constant streamwise vorticity enlarges together with its velocity magnitude. We can also observe that the area as well as the velocity magnitude of the swirl is increased with an increase in the AoA before the stall angle. For instance, at $\xi = 0.30$, the swirling area only occupies a quarter of the half-span with

the maximum velocity similar to the freestream value at $\alpha = 20.7°$. However, the swirling area increases to 50% of the half-span at $\xi = 0.24$ with the maximum velocity of 1.5 times the freestream value at $\alpha = 40.5°$. This is one of the reasons why the stall angle of the low AR flat plate is as high as $\alpha = 42°$.

Some other vorticities are seen between $\zeta = 0$ and $\zeta = 1$, which seem to come from the interaction of the TV with the LEV. The strength of those vorticities becomes much intense at $\alpha = 40.5°$ with an increase in the LEV strength, see Fig. 9. Moving downstream, the positive vorticity of the TV near the tip increases, inducing the secondary vorticity at the wing surface. Figure 10j at $\alpha = 30.6°$ and Fig. 10n at $\alpha = 40.5°$ indicate that the vorticity produced by the TV is extended from the tip towards the mid-span. Although the TV becomes greater in size at $\alpha = 50.4°$, the vorticity strength inside is much weaker than that at other AoAs. It is also moving away from the wing surface downstream.

The Reynolds stress ($-\overline{vw}/U_\infty^2$) in the y–z plane is presented in Fig. 11. The areas of high Reynolds stress are around the edge of the TV core, indicating an interaction
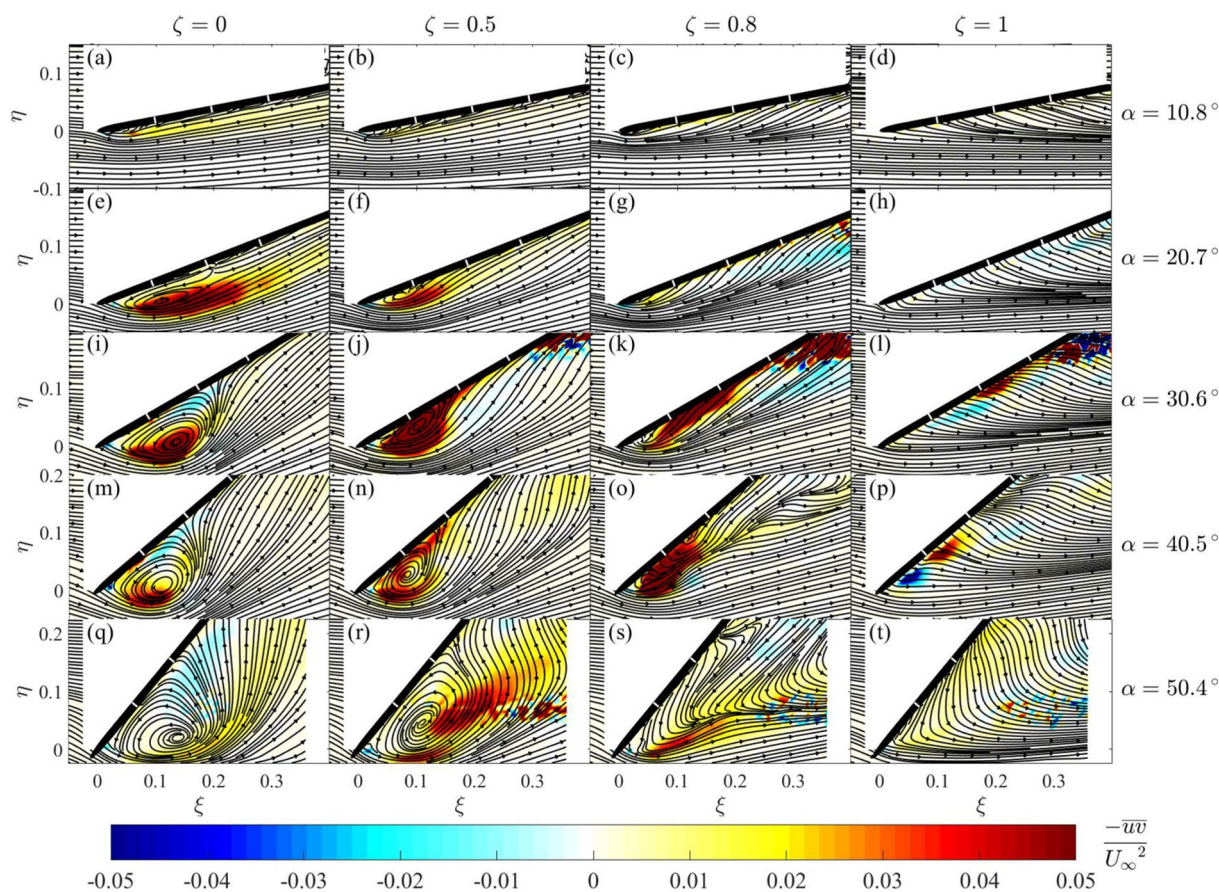
Fig. 8 Non-dimensional Reynolds stress $-\overline{uv}/U_\infty^2$ superimposed on the streamlines along the span from $\zeta = 0$ to $\zeta = 1$ at five AoAs ($\alpha = 10.8°$ to $50.4°$). White markers are shown in every 10% chord length along the wing
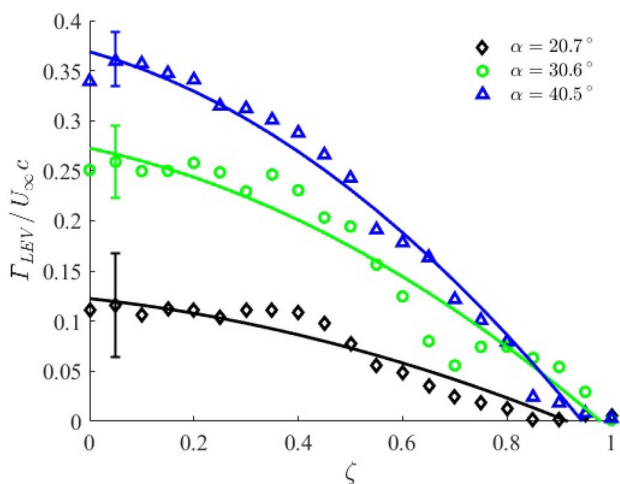

Fig. 9 Non-dimension LEV circulation ($\Gamma_{LEV}/U_\infty c$) of a thin wing along the span from $\alpha = 20.7°$ to $\alpha = 40.5°$. The error bar indicates a standard deviation of the measurement uncertainty

between the LEV and the TV. Downstream of the leading-edge, the Reynolds stress is reduced progressively without LEV, see Fig. 11l, o. At a small AoA, very weak Reynolds stress can be observed near the leading-edge, which is due to the weak LEV and TV. With an increase in the AoA, the TV becomes stronger, resulting in a greater turbulent mixing indicated by the high Reynolds stress shown here. After the stall at $\alpha = 50.4°$, a large separation area develops. Here, an intense interaction between the TV and the separated flow can be observed at $\xi = 0.15$ and $\xi = 0.20$ in Fig. 11s, t, respectively, showing a stronger mixing layer.

The Reynolds stress can still be observed inside the TV, which might be due to the effect of the vortex core wandering. Probability density functions (PDF) of 400 instantaneous TV centroids along the η-axis and ζ-axis at a distance of $0.35c$ along the wing chord from the leading-edge at three AoAs are presented in Fig. 12 to show this phenomenon, where $\triangle\eta$ and $\triangle\zeta$ are the centroid distance between the instantaneous and the time-averaged TV. The probability density functions of TV centroids are well represented by a Gaussian distribution (see Fig. 12), where the standard deviation (σ) increases with an increase in the AoA. Here, the
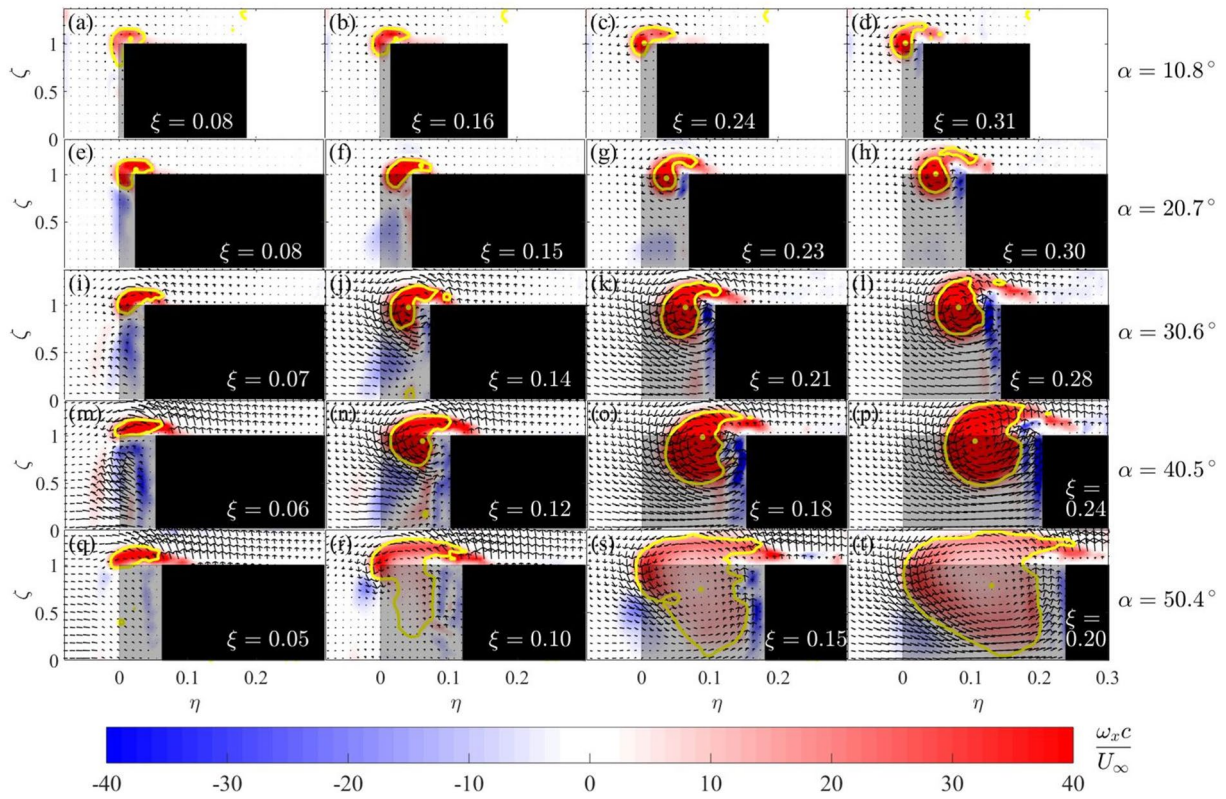
Fig. 10 Vorticity fields superimposed on the velocity vectors at different distance to leading-edge along the chord at five AoAs ($\alpha = 10.8°$ to 50.4°). The yellow lines and points in figure indicate the TVs and the centroids of the TVs identified by the λ_2–criteria, respectively

location of maximum probability has been slightly affected by the size of interrogation area ($0.0025c \times 0.0025c$) during the PIV analysis. This suggests that the degree of vortex wandering increases with the angle of attack, causing a higher C_L fluctuation at a higher AoA.

The non-dimensional streamwise circulation of the TV, $\Gamma_{TV}^* = \Gamma_{TV}/U_\infty c$ is shown in Fig. 13 for $\alpha = 10.8°$ to $\alpha = 50.4°$. At $\alpha = 0°$, Γ_{TV}^* is nearly zero because there is no TV. With an increase in the AoA until the stall Γ_{TV}^* increases monotonically. The figure also shows that the Γ_{TV}^* increases downstream. This suggests that a low AR thin wing is similar to a delta wing (Gordnier and Visbal 1994a; Ma et al. 2017b), where the circulation of the TV increases linearly with a downstream distance (Visser and Nelson 1993a; Traub 1997a). We can fit the experimental data as $\Gamma_{TV}^* = 3.72\alpha_r^{2.1}\xi$ up until the maximum lift angle, where α_r is the AoA in radians, see solid lines in Fig. 13. The relationship between the circulation and angle of attack is linear only for a small angle of attack. At a large AoA, there is an intense interaction between TV and LEV for $\xi < 0.12$, therefore the growth of circulation near the leading edge is different from the rest. After the stall

angle, the LEV becomes weaker, but the rate of increase in circulation becomes greater downstream, however, as can be seen in Fig. 13.

To characterise the development of the TV, the distance of the TV centroid to the wall (d) and the TV diameter (D) are obtained and shown in Fig. 14 in non-dimensional form. Figure 14a shows that the non-dimensional distance of the TV centroid to the wing (d/c) changes almost linearly along the chord, which can be represented by $d/c = 0.56e^{2.3\alpha_r}\xi$. Here, the vortex diameter is calculated by $D = 2 \times \sqrt{S_{con}/\pi}$, where S_{con} is area of the vortex core identified by λ_2, which is shown in Fig. 10. The non-dimensional diameter of the TV increases with an increase in the AoA, which can be fitted to an expression given by $\frac{D}{c} = 0.027e^{2.78\alpha_r}\sqrt{\xi}$, see Fig. 14b. This relationship is expected since the circulation of the TV with a constant vorticity core is proportional to D^2, which linearly increases with ξ as shown in Fig. 13. Near the leading-edge, the development of the TV is affected by the LEV, therefore, the data do not fit to these expressions very well. We expect the proportional constants in the expressions for d/c and D/c are function of the aspect ratio AR of the wing
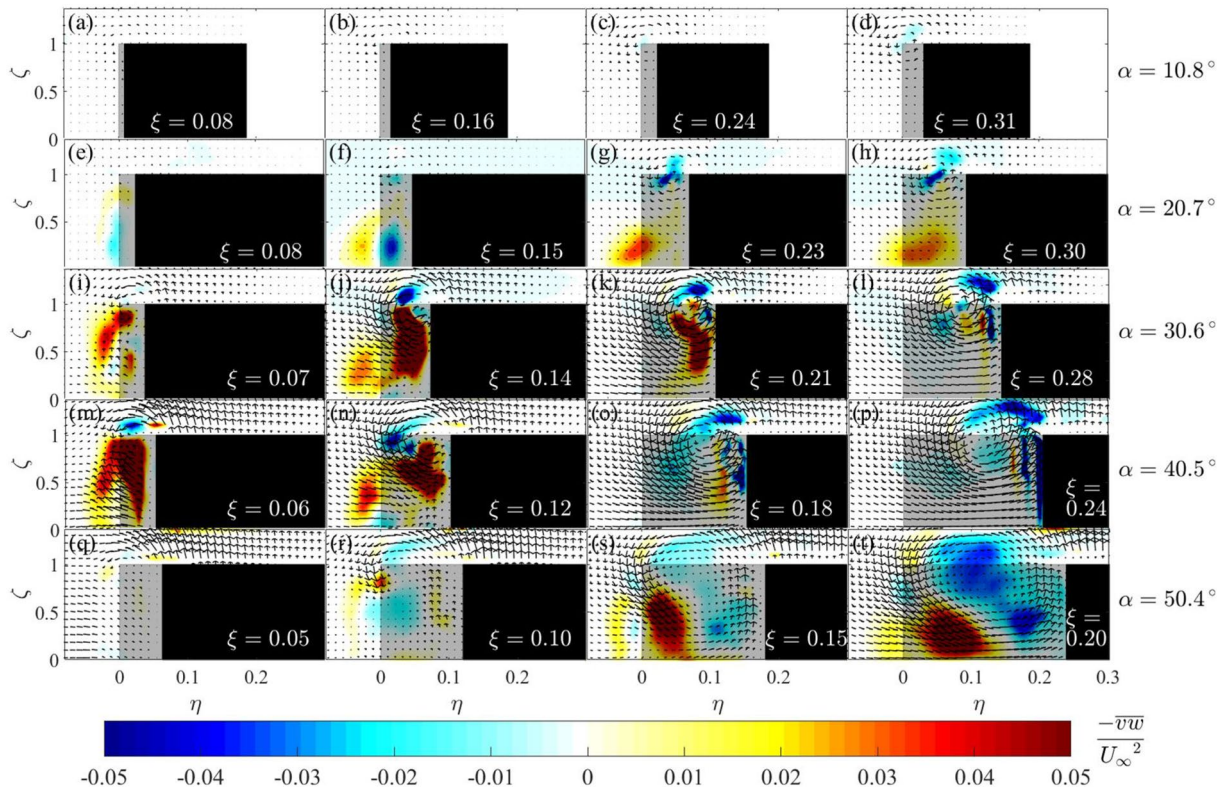
Fig. 11 Non-dimensional Reynolds stress $-\overline{vw}/U_\infty^2$ superimposed on the velocity vectors along the chord at five AoAs ($\alpha = 10.8°$ to $50.4°$)
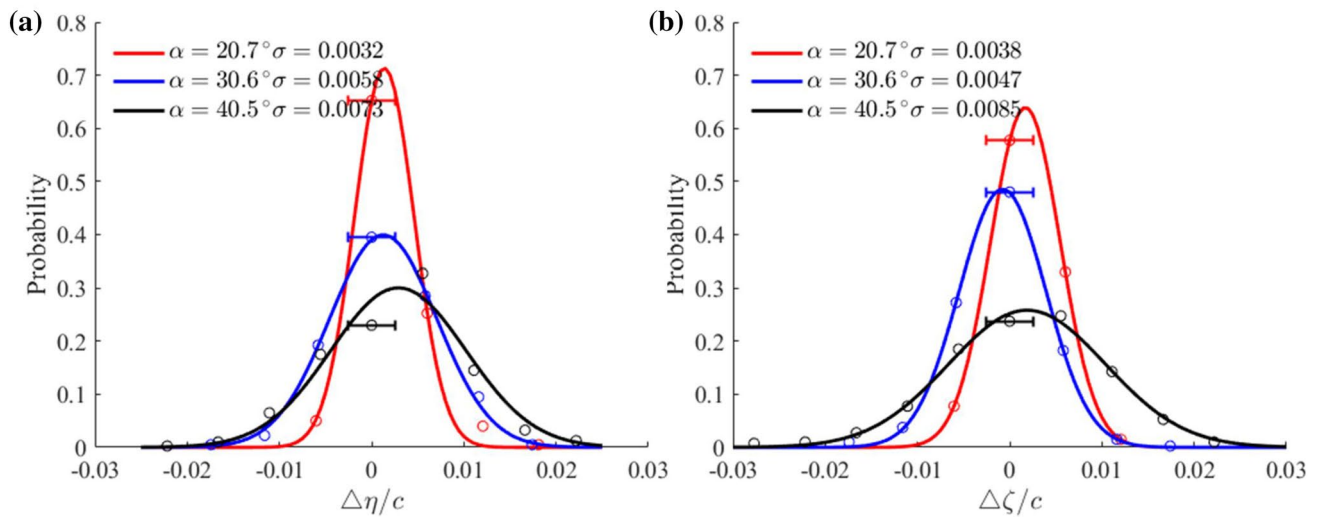

Fig. 12 Probability density functions of the 400 instantaneous TV centroid at $0.35c$ from the leading edge along the wing chord at three AoAs: **a** the wandering of the TV centroid along the η-axis; **b** the wandering of the TV centroid along the ζ-axis. The error bar indicates the size of interrogation area for the calculation of PDF
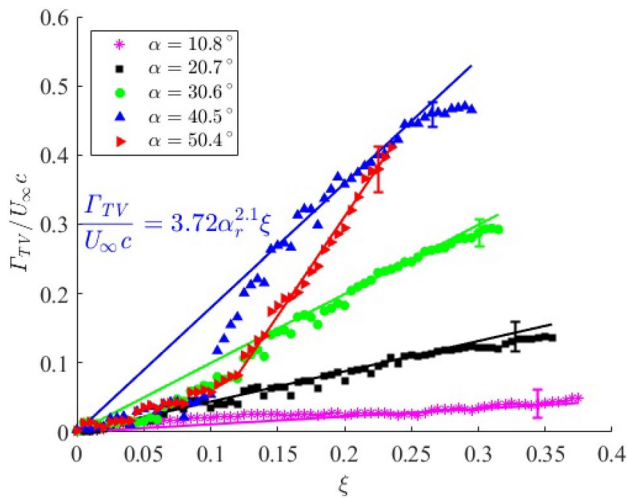
Fig. 13 Streamwise circulation Γ_{TV} along ξ from $\alpha = 10.8°$ to $50.4°$, the fitted curves ($\Gamma_{TV}/U_\infty c = 3.72\alpha_r^{2.1}\xi$) are shown in solid lines. The error bar indicates a standard deviation of the measurement uncertainty

as well as the Re. It is noted that the TV diameter increases much faster after the stall angle.

3.4 The induced velocity of the TV

We showed in Figs. 4 and 5 that the flow separates at the leading-edge and then reattaches to the wing surface, forming the LEV. To quantify the flow behaviour of this leading-edge separation region, we define the separation length (SL) as the distance between the leading-edge and the reattachment point along the wing chord where the probability of forward flow and reversed flow becomes

equal (Kasagi and Matsunaga 1995). This is shown in Fig. 15 along the span. Only results at three AoAs are presented here, where the separation region can be identified unambiguously. The non-dimensional separation length SL/c takes maximum at the mid-span ($\zeta = 0$) and reduces to zero towards the tip edge. At a small angle of attack ($\alpha = 20.7°$), SL/c reduces nearly linearly with ζ. With an increase in the AoA, however, the rate of reduction in SL/c with ζ is less as shown in Fig.15, although the maximum value in *SL/c* is smaller. The induced velocity of the TV helps suppress the separation around the leading-edge for a low AR wing, thereby increasing the maximum lift angle to 42° (see Fig. 3).

To investigate how the leading-edge flow separation is influenced by the TV, the induced velocity (U_d) at three AoAs is computed and presented in Fig. 16 together with the streamlines near the leading-edge. Here, we assumed that the TV can be represented by a Rankine vortex and neglected the interaction between TV and LEV near the leading edge. There is a strong correlation between the reattachment point and the region of large induced velocity in Fig. 16. In other words, the reattachment point moves upstream with an increase in the induced velocity. The variation of the span-averaged value of induced velocity (U_m) along the streamwise direction is presented in Fig. 17 together with the reattachment points of the LEV. The results in the figure show that the spanwise-averaged induced velocity is given by $(0.16 \pm 0.032)U_\infty$ at $\alpha = 20.7°$, while it is $(0.39 \pm 0.023)U_\infty$ at $\alpha = 30.6°$ and $(0.59 \pm 0.037)U_\infty$ at $\alpha = 40.5°$. These results suggest that the induced velocity of the TV should reach a certain required value to suppress a leading edge flow separation. With an increase in the AoA, this required value of induced velocity increases due to an
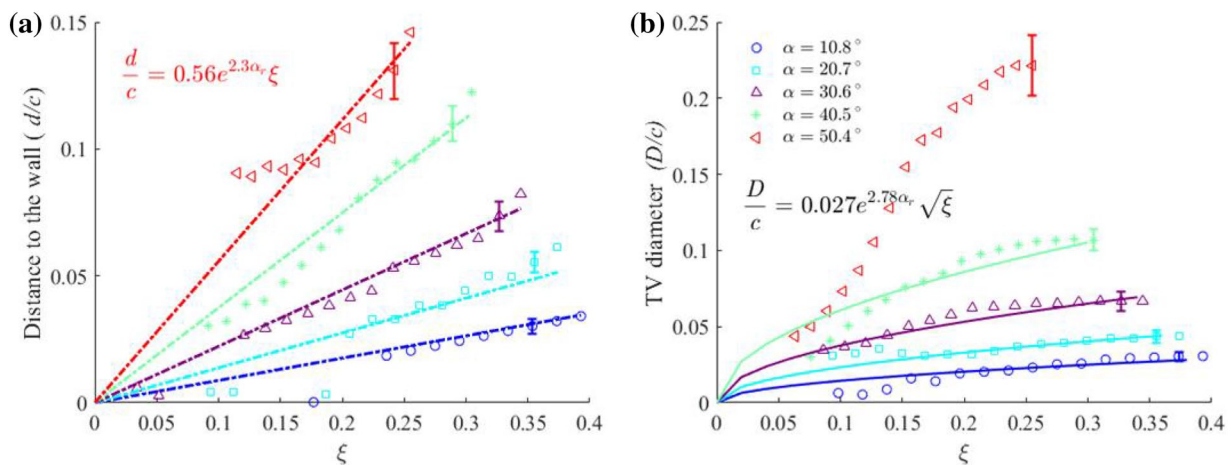

Fig. 14 TV's centroid positions (**a**) and diameters (**b**) along ξ at different AoAs. The error bar indicates a standard deviation of the measurement uncertainty
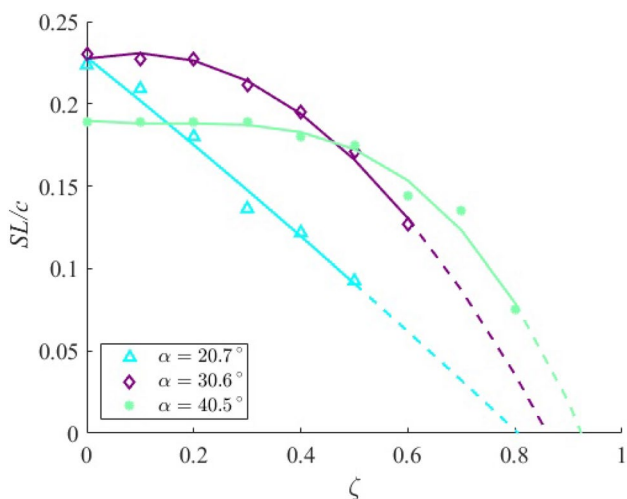
Fig. 15 Separation length and the reattachment point along the span from $\alpha = 20.7°$ to $40.5°$

increased separation region. When the induced velocity of the TV cannot reach the required value with a further increase in the AoA, separated flow cannot be reattached, resulting in the stall (Fig. 5q–t).

Overall, the fundamental reason for a great C_L and a large stall angle on a low AR wing is that the induced velocity from TV can suppress and reattach the separated flow near the leading edge. This results in a formation of LEV which has an important contribution to the lift. With an increase in

the AoA, the induced velocity due to TV increases, which can suppress and reattach the separated flow more efficiently. Our result should help design MAVs that require a large stall angle and better understand the flight physics of natural flyers whose wings have low AR.

4 Conclusions

We have investigated the interplay between the leading-edge vortex and the tip vortex over a low aspect-ratio thin wing using PIV and force measurements. We found that the circulation of the leading-edge vortex increases with an increase in the angle of attack. The contribution of the leading-edge vortex on the total lift is approximately 30% at $\alpha = 20.7°$ to $40.5°$. The reattachment of leading-edge flow and the subsequent formation of the leading-edge vortex is due to the induced velocity by the tip vortex. Induced velocity of the tip vortex increases with an increase in the angle of attack. After the stall angle, the tip vortex starts to expand and detaches from the wing surface, resulting in a large flow separation. Vortex interactions are found near the leading-edge, corresponding to the intense turbulent mixing indicated by high Reynolds stress. The circulation, core position and diameter of the tip-vortex are obtained and expressed in terms of the angle of attack and the distance from the leading-edge. Meanwhile, The vortex wandering phenomenon of the tip vortex is observed, affecting the stability of the low aspect-ratio thin wing.
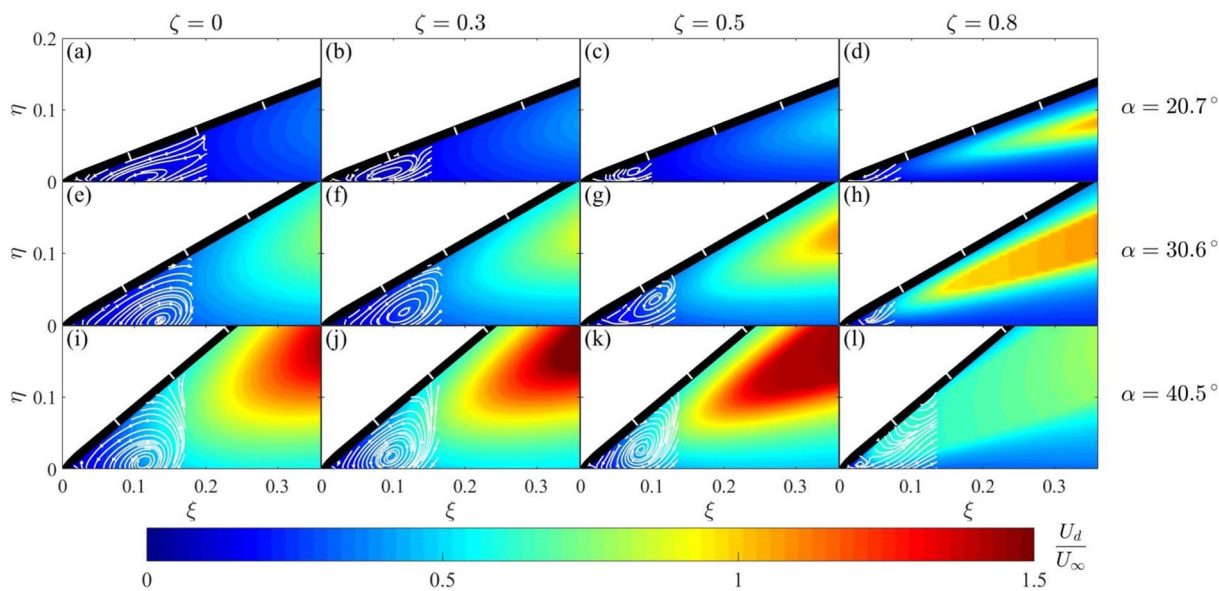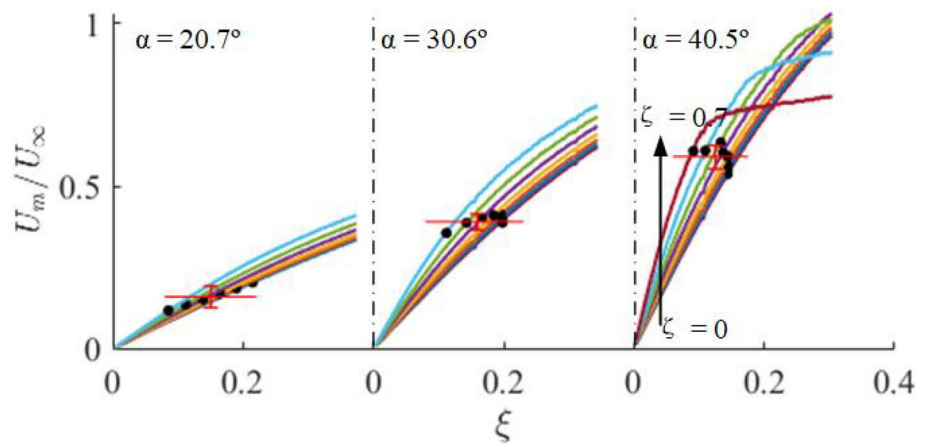

Fig. 16 The induced velocity distribution superimposed on the separated flow streamlines from the mid-span ($\zeta = 0$) to tip-edge ($\zeta = 0.8$) at $\alpha = 20.7°$, $\alpha = 30.6°$ and $\alpha = 40.5°$. White markers are shown in every 10% chord length along the wing

Fig. 17 Variations of the spanwise-averaged induced velocity from $\zeta = 0$ to $\zeta = 0.7$ at $\alpha = 20.7°$, $\alpha = 30.6°$, and $\alpha = 40.5°$. The solid points indicate the reattachment points along the span

References

Baik YS, Bernal LP, Granlund K, Ol MV (2012) Unsteady force generation and vortex dynamics of pitching and plunging aerofoils. J Fluid Mech 709:37–68. https://doi.org/10.1017/jfm.2012.318

Bohl DG, Koochesfahani MM (2009) MTV measurements of the vortical field in the wake of an airfoil oscillating at high reduced frequency. J Fluid Mech 620:63–88. https://doi.org/10.1017/S0022112008004734

Bomphrey RJ, Taylor GK, Thomas AL (2009) Smoke visualization of free-flying bumblebees indicates independent leading-edge vortices on each wing pair. Exp Fluids 46:811–821. https://doi.org/10.1007/s00348-009-0631-8

Carr Z, Chen C, Ringuette M (2013) Finite-span rotating wings: three-dimensional vortex formation and variations with aspect ratio. Exp Fluids 54(2):1444. https://doi.org/10.1007/s00348-012-1444-8

Chandrsuda C, Bradshaw P (1981) Turbulence structure of a reattaching mixing layer. J Fluid Mech 110:171–194. https://doi.org/10.1017/S0022112081000670

DeVoria AC, Mohseni K (2017) On the mechanism of high-incidence lift generation for steadily translating low-aspect-ratio wings. J Fluid Mech 813:110–126. https://doi.org/10.1017/jfm.2016.849

Gordnier RE, Visbal MR (1994) Unsteady vortex structure over a delta wing. J Aircr 31(1):243–248. https://doi.org/10.2514/3.46480

Granlund K, Ol M, Bernal L (2011) Experiments on free-to-pivot hover motions of multi-hinged flat plates. In: AIAA atmospheric flight mechanics conference, p 6527. https://doi.org/10.2514/6.2011-6527

Hartloper C, Kinzel M, Rival DE (2013) On the competition between leading-edge and tip-vortex growth for a pitching plate. Exp Fluids 54(1):1447. https://doi.org/10.1007/s00348-012-1447-5

Jeong J, Hussain F (1995) On the identification of a vortex. J Fluid Mech 285:69–94. https://doi.org/10.1017/S0022112095000462

Jian T, Ke-Qin Z (2004) Numerical and experimental study of flow structure of low-aspect-ratio wing. J Aircr 41(5):1196–1201. https://doi.org/10.2514/1.5467

Jiang M, Machiraju R, Thompson D (2005) Detection and visualization of vortices. In: The visualization handbook, p 295

Kasagi N, Matsunaga A (1995) Three-dimensional particle-tracking velocimetry measurement of turbulence statistics and energy budget in a backward-facing step flow. Int J Heat Fluid Flow 16(6):477–485. https://doi.org/10.1016/0142-727X(95)00041-N

Kine S, McClintock F (1953) Describing uncertainties in single-sample experiments. Mech Eng 75:3–8

LeMay S, Batill S, Nelson R (1990) Vortex dynamics on a pitching delta wing. J Aircr 27(2):131–138. https://doi.org/10.2514/3.45908

Ma BF, Wang Z, Gursul I (2017) Symmetry breaking and instabilities of conical vortex pairs over slender delta wings. J Fluid Mech 832:41–72. https://doi.org/10.1017/jfm.2017.648

Madnia CK (2010) Review of "fundamentals of aerodynamics". AIAA J 48(12):2983–2983. https://doi.org/10.2514/1.52157

McCroskey WJ (1982) Unsteady airfoils. Annu Rev Fluid Mech 14(1):285–311. https://doi.org/10.1146/annurev.fl.14.010182.001441

Mueller TJ, Batill SM (1982) Experimental studies of separation on a two-dimensional airfoil at low Reynolds numbers. AIAA J 20(4):457–463. https://doi.org/10.2514/3.51095

Ohmi K, Coutanceau M, Daube O, Loc TP (1991) Further experiments on vortex formation around an oscillating and translating airfoil at large incidences. J Fluid Mech 225:607–630. https://doi.org/10.1017/S0022112091002197

Pelletier A, Mueller TJ (2000) Low Reynolds number aerodynamics of low-aspect-ratio, thin/flat/cambered-plate wings. J Aircr 37(5):825–832. https://doi.org/10.2514/2.2676

Rossow VJ (1978) Lift enhancement by an externally trapped vortex. J Aircr 15(9):618–625. https://doi.org/10.2514/3.58416

Shyy W, Liu H (2007) Flapping wings and aerodynamic lift: the role of leading-edge vortices. AIAA J 45(12):2817–2819. https://doi.org/10.2514/1.33205

Storms BL, Jang CS (1994) Lift enhancement of an airfoil using a gurney flap and vortex generators. J Aircr 31(3):542–547. https://doi.org/10.2514/3.46528

Taira K, Colonius T (2009) Three-dimensional flows around low-aspect-ratio flat-plate wings at low Reynolds numbers. J Fluid Mech 623:187–207. https://doi.org/10.1017/S0022112008005314

Torres GE, Mueller TJ (2004) Low aspect ratio aerodynamics at low Reynolds numbers. AIAA J 42(5):865–873. https://doi.org/10.2514/1.439

Traub LW (1997) Prediction of delta wing leading-edge vortex circulation and lift-curve slope. J Aircr 34(3):450–452. https://doi.org/10.2514/2.2193

Visbal MR (1994) Onset of vortex breakdown above a pitching delta wing. AIAA J 32(8):1568–1575. https://doi.org/10.2514/3.12145

Visser K, Nelson R (1993) Measurements of circulation and vorticity in the leading-edge vortex of a delta wing. AIAA J 31(1):104–111. https://doi.org/10.2514/3.11325

Von Ellenrieder KD, Pothos S (2008) PIV measurements of the asymmetric wake of a two dimensional heaving hydrofoil. Exp Fluids 44(5):733–745. https://doi.org/10.1007/s00348-007-0430-z

Von Ellenrieder KD, Parker K, Soria J (2003) Flow structures behind a heaving and pitching finite-span wing. J Fluid Mech 490:129–138. https://doi.org/10.1017/S0022112003005408

Wang ZJ (2005) Dissecting insect flight. Annu Rev Fluid Mech 37:183–210. https://doi.org/10.1146/annurev.fluid.36.050802.121940

Wang S, Zhou Y, Alam MM, Yang H (2014) Turbulent intensity and Reynolds number effects on an airfoil at low Reynolds numbers. Phys Fluids 26(11):115107. https://doi.org/10.1063/1.4901969

Warrick DR, Tobalske BW, Powers DR (2005) Aerodynamics of the hovering hummingbird. Nature 435(7045):1094–1097. https://doi.org/10.1038/nature03647

Westerweel J (1997) Fundamentals of digital particle image velocimetry. Meas Sci Technol 8(12):1379. http://iopscience.iop.org/0957-0233/8/12/002

Westerweel J, Scarano F (2005) Universal outlier detection for PIV data. Exp Fluids 39(6):1096–1100 https://doi.org/10.1007/s00348-005-0016-6

Willert CE, Gharib M (1997) The interaction of spatially modulated vortex pairs with free surfaces. J Fluid Mech 345:227–250. https://doi.org/10.1017/S0022112097006265

Winter H (1936) Flow phenomena on plates and airfoils of short span

Yilmaz TO, Rockwell D (2012) Flow structure on finite-span wings due to pitch-up motion. J Fluid Mech 691:518–545. https://doi.org/10.1017/jfm.2011.490